International Journal of Modern Manufacturing Technologies
ISSN 2067–3604, Vol. XIV, No. 1 / 2022
https://doi.org/10.54684/ijmmt.2022.14.1.33

STRUCTURAL CHANGES IN A POWDER METALLURGY 66FE-14MN-6SI-9CR-5NI (MASS. %) SHAPE MEMORY ALLOY SUBJECTED TO BENDING CREEP

Lenuța Ciurcă, Bogdan Pricop, Maricel Agop, Leandru-Gheorghe Bujoreanu

Faculty of Materials Science and Engineering, „Gheorghe Asachi" Technical University of Iași,
Blvd. Dimitrie Mangeron 61A. 700050 Iași, Romania

Corresponding author: Leandru-Gheorghe Bujoreanu, leandru-gheorghe.bujoreanu@academic.tuiasi.ro

Abstract: Fe-14Mn-6Si-9Cr-5Ni (mass. %) shape memory alloy (SMA) has been developed as a commercial grade of Fe-Mn-Si based SMAs with excellent formability and corrosion resistance. Producing FeMnSiCrNi SMAs by powder metallurgy enables a better control of chemical composition and grain size. This paper discusses the variation of bending creep deformation, as a function of time, temperature and force, in the case of a powder metallurgy (PM) Fe-14Mn-6Si-9Cr-5Ni SMA with 50 % mechanically alloyed powder volume. Creep test temperatures were selected based on phase transitions determined by dynamic mechanical analysis (DMA), during heating. The results suggested the tendency of martensite plate variants to reorient along a common direction, after creep.

Key words: FeMnSiCrNi shape memory alloy, martensite, bending creep, creep rate.

1. INTRODUCTION

The alloy with chemical composition 66Fe-14Mn-6Si-9Cr-5Ni (mass. %, as listed herein after, unless differently stated) was developed with the aim to induce corrosion resistance (by Cr additions) and to avoid the formation of harmful σ-phase (by Ni additions) in Fe-Mn-Si based shape memory alloys (SMAs) [1]. It was pointed out that the alloy can be hot rolled with total reduction degrees up to 80 %, without cracking, which enabled an ultimate strain up to 72 %, during tensile failure tests [1]. Thus, FeMnSiCrNi SMAs have been recognized as corrosion resistant, with the capacity to accommodate high recovery strains, reaching 7.7 % in the case of an as-cast Fe-19Mn-5.5Si-9Cr-4.5Ni alloy with an average grain size above 0.6 mm [3]. Based on these characteristics, practical applications were devised. For instance, an Fe–15Mn–5Si–9Cr–5Ni SMA was used to produce pipe couplings [4] and an Fe 15Mn 4Si 10Cr 8Ni alloy to manufacture anti-seismic dampers for the protection of an 196-metre skyscraper [5].
One alternative processing routine, of FeMnSiCrNi SMAs, has been powder metallurgy (PM) comprising mechanically alloyed (MA'ed) particles [6]. Using PM-MA combinations, it was argued that high rate actuators [7] and pipe couplings for turbulent fluid transportation [8] could be manufactured from Fe-14Mn-6Si-9Cr-5Ni SMAs.
The previous studies, reported by some of the present authors, concerned tensile and bending creep behaviours of a PM Fe-18Mn-3Si-7Cr-4Ni. The former enabled to determine second order polynomial fits for the saturation tendencies of permanent and total strains recorded during 100 tensile loading-unloading cycles up to 600 MPa [9]. The latter revealed the stabilization of secondary creep stage, with bending deflection rates as a function of time and temperature ranging between 4.77×10^{-6} and 9.35×10^{-6} $\mu m/(s\times{}^0C)$, and the validation of a proposed multifractal hydrodynamic model [10].
In this context, the present work was directed to the experimental study of creep phenomena occurring in a PM Fe-14Mn-6Si-9Cr-5Ni SMA subjected to three-point-bending and to the modeling of its behavior.

2. MATERIALS AND METHODS

Elemental powders with the nominal chemical composition 66Fe-14Mn-6Si-9Cr-5Ni were mixed in a turbula blender. Then, 50 vol % of the powders were mechanically alloyed in a SPEXTM D8000 high energy ball mill using stainless steel vials and stainless-steel milling balls [11]. The process was performed under argon atmosphere, for 4 h, with 3 wt.% addition of Stearic Acid and a ball-to-powder ratio of 1/ 10 [12]. Sintering was performed under argon atmosphere, at 1150^0C for 2 h using high-temperature furnace and H_2 insertion at 800^0C for 30 min, in order to reduce the oxides from samples. Pressing was achieved at 500 MPa, by means of an uniaxial hydraulic press and used a rectangular prism mold with 4×40 cross section [13]. Sintered parallelepipedic billets were further hot rolled

at 1060^{0}C by means of a laboratory roller, until thickness decreased to approx. 1 mm [14]. By wire spark erosion, performed on a DEM 320 A machine with 0.18 mm-diameter molybdenum wire, rectangular specimens were cut and ground to remove superficial oxides. The specimens, with final dimensions 50×4×1 mm were used for dynamic mechanical analysis (DMA). Temperature scans, from room temperature to 400^{0}C with 5^{0}C /min heating rate and 1 Hz frequency as well as creep tests, by 2000s-bending under different constant forces and temperatures were achieved with a NETZSCH DMA 242 Artemis analyser. A dual cantilever (DCL) specimen holder, shown in Figure 1 and PROTEUS software were used, for this purpose. All experimental details were previously provided [10].

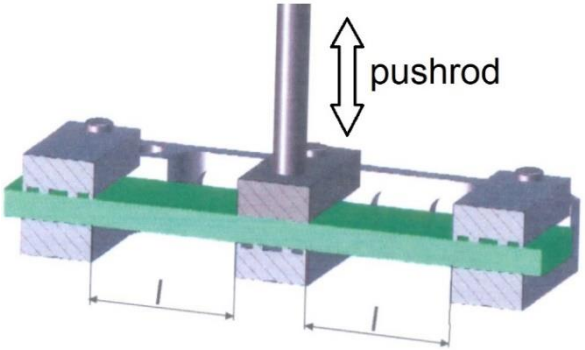

Fig. 1. Schematic representation of DCL specimen holder used during DMA experiments

Microstructural changes, produced after creep, were analysed by means of optical (OM) and scanning electron microscopy (SEM). In this purpose, the specimens were ground, polished and etched with a solution of 1.2% $K_2S_2O_5$ + 1% NH_4HF_2 in 100 ml distilled water. OM micrographs were recorded with an OPTIKA XDS-3 MET microscope equipped with an OPTIKAM 4083.B5 microscope, a digital USB camera, and an OPTIKAM B5 software. SEM observations were performed with a VEGA II LMH TESCAN scanning electron microscope equipped with an EDX-QUANTAX QX2 ROENEC energy-dispersive spectrometer and ESPRIT 1.8 software.

3. RESULTS AND DISCUSSION

The representative results of DMA thermal scans may be summarized by the variation of internal friction, tan δ= E"/ E' (E'-storage modulus and E"-loss modulus) with temperature, illustrated in Figure 2.
In our opinion, the two tan δ maxima are related to antiferromagnetic ⇒ paramagnetic transition, superimposed over the reverse martensitic transformation of α'-body centred cubic (bcc) martensite which retransforms to γ-face centred cubic (fcc) austenite and to the reverse martensitic transformation of to ε-hexagonal close packed (hcp) martensite which reverses to γ-fcc austenite [6,8]. Following the same approach as in our previous study [10], five temperatures were designated in Figure 2, corresponding to as many states: 1-60^{0}C, low temperature fully antiferromagnetic martensite state; 2-200^{0}C, high temperature antiferromagnetic and partially paramagnetic martensite state; 3-242^{0}C, half antiferromagnetic martensite-half paramagnetic martensite state; 4-274^{0}C, half paramagnetic martensite-half austenite state; 5-300^{0}C, fully austenite state.

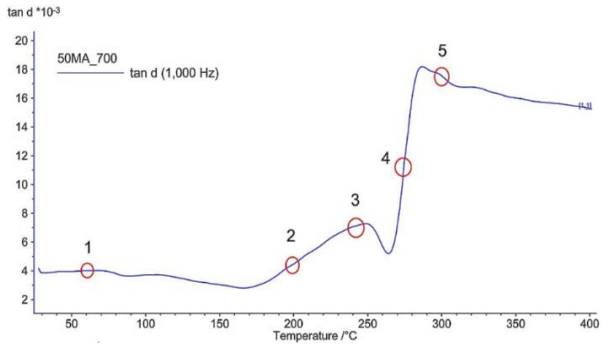

Fig. 2. DMA thermogram of the variation of internal friction (tan δ) with temperature, during heating of a PM Fe-14Mn-6Si-9Cr-5Ni (mass. %) SMA

3.1 Creep behaviour

As in our previous study, the experimental approach for low-temperature creep and stress relaxation behaviour was applied [15] and the creep and relaxation variant of PROTEUS software was used [10]. The procedure consists in bending four specimens at four different forces, respectively, for 2000 s, then in unloading and straightening the specimens, to zero deflection and in heating them to the next temperature, from the above mentioned list. Maximum force cannot exceed 12 N for self-protection reasons. Experimental data consisted in bending deflection as a function of time, at four force (1, 3, 6 and 9 N) and five above mentioned temperature (60, 200, 242, 274 and 300^{0}C) values, illustrated in Figure 3.

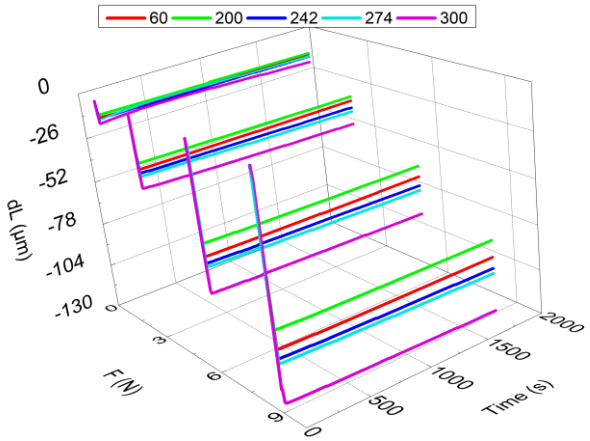

Fig. 3. Variation of bending deflection in time, at five testing temperatures (mentioned in ^{0}C) and four bending forces (1, 3, 6 and 9 N, respectively)

In Figure 3, dL represents the bending deflection of the specimen and has negative values because the pushrod moves downwards and PROTEUS software recognizes this deformation as a compression.

As in the previous study, creep deformation occurred in two stages: (i) primary, with high deformation rate and (ii) secondary with very low deformation rate. Secondary creep rates are much lower than primary creep rates because, in this stage, a compensation mode is reached between dislocation annihilation and multiplication, in such a way that dislocation density is kept almost constant [16].

With a single exception, creep deformation monotonically increased with applied force and test temperature. The exception consists in obtaining the lowest creep deformations at 200^0C, in the high temperature antiferromagnetic and partially paramagnetic martensite state than at room temperature, in fully antiferromagnetic martensite state.

In other words, the creep deformation of martensite has been higher when a part of antiferromagnetic phase transformed to paramagnetic phase at 200^0C. It is noticeable that, in the case of 9 N applied force, creep deformation at 200^0C was more than 10 μm lower than that obtained at 60^0C.

In our opinion, this phenomenon could be caused by shape memory effect (SME), which tends to recover the original shape by straightening the specimen, but also to the decomposition of α'-bcc martensite, within this temperature range [17].

It is obvious that passing from half antiferromagnetic martensite-half paramagnetic martensite state, at 242^0C, to half paramagnetic martensite-half austenite state, at 274^0C, caused only a slight increase of creep deformation, while full austenite state, at 300^0C, obviously caused the largest deflections, exceeding 125 μm under an applied force of 9 N.

These results are slightly different from those reported in the case of a PM Fe-18Mn-3Si-7Cr-4Ni where, in the same conditions, maximum deflection reached 100 μm [10]. So, it appears that decreasing Mn amount from 18 to 14 wt. % caused a noticeable increase of creep deformation.

After fitting both primary and secondary creep regions, from Figure 3, with linear functions, the respective slopes were assimilated with creep rates and illustrated in Figure 4.

It is noticeable, in Figure 4(a), that primary creep rates monotonically increased with the applied force, from 1 to 8 μm/s. With increasing test temperature, from 60 to 200^0C, primary creep rate slightly decreased, possibly due to SME occurrence. Further increase of test temperature caused slight creep rate increases, reaching a maximum of 9.7 μm/s, at 300^0C, for an applied force of 9 N.

As previously reported for PM Fe-18Mn-3Si-7Cr-4Ni, secondary creep rates were typically three orders of magnitude lower than primary creep ones [10]. Thus, in Figure 4(b), for 1 N applied force, secondary creep rate reached 1.5 nm/s for the test temperature of 300^0C. On the other hand, increasing the values of applied force, from 3 to 9 N, seems to have no effect on secondary creep rate since the variation curves are overlapping, for test temperatures between 60 and 274^0C, where the average rate increased from 0.75 nm/s to 2 nm/s, respectively.

So, it is rather obvious, that secondary creep has been stabilized, up to 274^0C. The situation is quite different at 300^0C, where secondary creep rates range between approx. 1.5 and 2.5 nm/s.

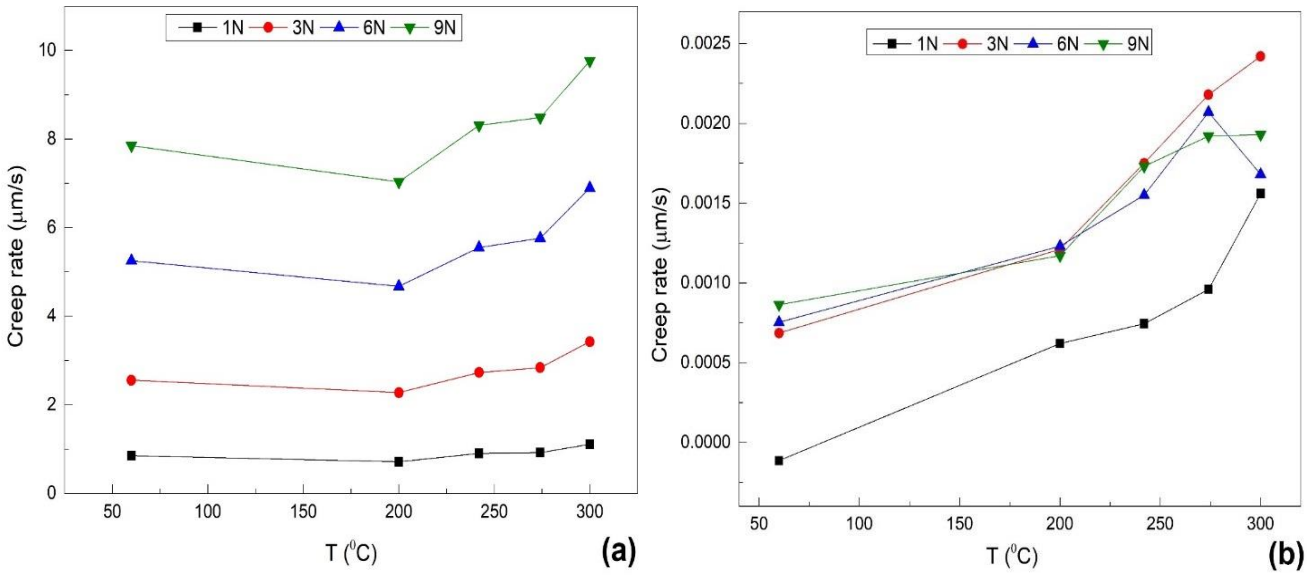

Fig. 4. Creep rate variation with temperature, under four different applied forces, obtained from linear fitting of the two creep regions from Figure 3: (a) primary creep; (b) secondary creep

Table 1. Results of linear fitting of secondary creep rate variation, [y, μm/(s)], with temperature (x, ^{0}C), from Figure 4(b)

Applied bending force	1 N	3 N	6 N	9 N
Equation	$y = a + b \cdot x$			
Intercept, *a* (μm/s)	$-5.55595\times10^{-4} \pm 2.68421\times10^{-4}$	$1.07692\times10^{-4} \pm 2.98032\times10^{-4}$	$4.29661\times10^{-4} \pm 2.91214\times10^{-4}$	$4.90257\times10^{-4} \pm 2.28922\times10^{-4}$
Slope, *b* [μm/(s×^{0}C)]	$6.0847\times10^{-6} \pm 1.16105\times10^{-6}$	$7.16228\times10^{-6} \pm 1.28913\times10^{-6}$	$4.77138\times10^{-6} \pm 1.25964\times10^{-6}$	$4.79722\times10^{-6} \pm 9.90197\times10^{-7}$
Residual Sum of Squares	1.44313×10^{-7}	1.7791×10^{-7}	1.69862×10^{-7}	1.04966×10^{-7}
Pearson's r	0.94949	0.95468	0.90943	0.94163
Adj. R-Square	0.8687	0.88189	0.76943	0.84889

As in the case of PM Fe-18Mn-3Si-7Cr-4Ni, secondary creep rates varied almost linearly with temperature. This observation suggested a linear fit of the secondary creep rate as a function of temperature. Thus, creep rate (y) was approximated as a linear function, under the form $y = a + bx$, where a represents theoretical secondary creep rate at 0^0C temperature and b the creep rate as a function of time and temperature. Table 1 lists the resulting values.

It is noticeable that the coefficient b, representing the slope of the linear fit, can be identified as the secondary creep rate as a function of time and temperature. As compared to PM Fe-18Mn-3Si-7Cr-4Ni, where theoretical secondary creep rate with time and temperature ranged between 4.77×10^{-6} and 9.35×10^{-6} μm/(s×^{0}C), in the case of the alloy under study it extents between 3.51×10^{-6} and 8.45×10^{-6} μm/(s×^{0}C). These values suggest that secondary creep is even more stabilized in PM-MA Fe-14Mn-6Si-9Cr-5Ni than it was in PM Fe-18Mn-3Si-7Cr-4Ni.

3.2 Microstructural evaluation of creep effects

Figure 5(a) illustrates the martensitic structure of 50 % mechanically alloyed (MA'ed) PM Fe-18Mn-3Si-7Cr-4Ni specimen in initial condition. As pointed out by white arrows, there are four different crystallographic directions of the orientation of martensite plates, which are typically aligned along the normal of $\{111\}_\gamma$ close packed planes [18]. These aspects are better illustrated by SEM micrograph, shown in Figure 5(b).

On the other hand, after 2000s of bending under the effects of a 9 N force applied at 300^0C, martensite plates showed two tendencies: (i) to reorient along a common direction and (ii) to decrease their heights, as noticeable from Figure 6. Thus the SEM micrograph from Figure 6(b) clearly shows a great majority of martensite plates with a single crystallographic orientation.

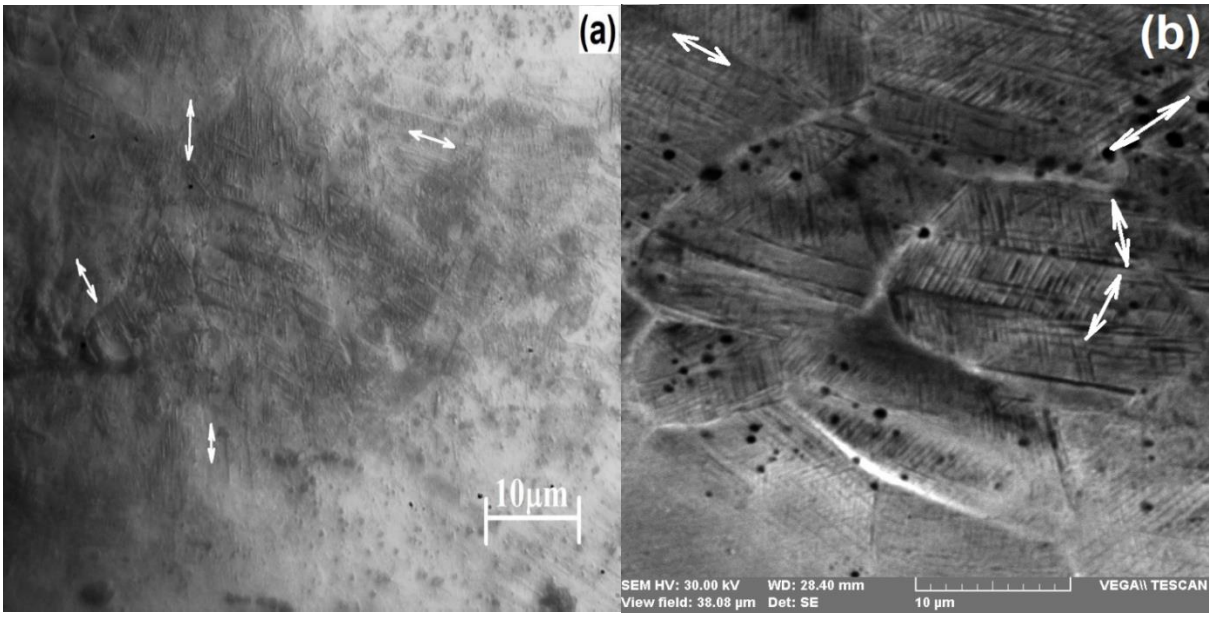

Fig. 5. Morphological details of martensite plates, illustrating at least four crystallographic orientations, in initial condition: (a) OM micrograph; (b) SEM micrograph

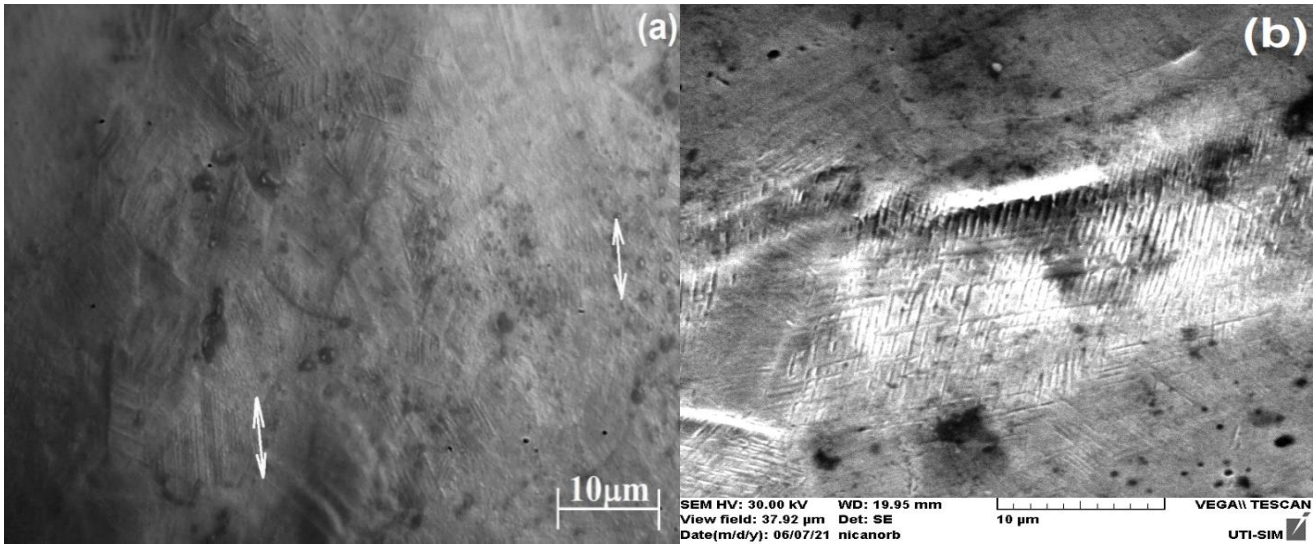

Fig. 6. Morphological details of martensite plates, illustrating an orientation tendency along an unique crystallographic orientation, after 2000 s bending creep at 300^0C: (a) OM micrograph; (b) SEM micrograph

4. CONCLUSIONS

The main conclusions of the present paper are stated below.

The hot rolled specimens of PM Fe-14Mn-6Si-9Cr-5Ni SMA with 50 % mechanically alloyed powder volume experienced a two-stage creep when subjected to bending. Its secondary creep has been more stabilized as compared to previously studied PM Fe-18Mn-3Si-7Cr-4Ni [10]. At PM Fe-14Mn-6Si-9Cr-5Ni SMA with 50 % mechanically alloyed powder the lowest creep deformations were obtained at 200^0C where a part of the bending deformation was recovered by shape memory effect. The secondary creep rates ranged between 3.51174 and 8.45141 × 10^{-6} μm/ (s×^{0}C). At the specimen which was subjected to bending creep at 300^0C, for 2000 s, under a load of 9 N, the tendency of martensite plates to align along a common direction was observed by optical and scanning electron microscopy.

5. REFERENCES

1. Otsuka H., Yamada H., Maruyama T., Matsuda S., Murakami M., (1990). *Effects of Alloying Additions on Fe-Mn-Si Shape Memory Alloys*, ISIJ Int, **30**, 674-679.

2. Moriya Y., Kimura H., lshizaki S., Hashizume S., Suzuki S., Suzuki H., Sampei T., (1991). *Properties of Fe-Cr-Ni-Mn-Si (-Co) shape memory alloys*, J Phys IV, France **01** C4, 433-437.

3. Peng H., Wang G., Wang S., Chen J., Mac Laren I., Wen Y., (2018). *Key criterion for achieving giant recovery strains in polycrystalline Fe-Mn-Si based shape memory alloys*. Mater. Sci. Eng. A. **712**, 37–49. doi: 10.1016/j.msea.2017.11.071.

4. Druker A., Perotti A., I. Esquivel, Malarría J., (2014). *A manufacturing process for shaft and pipe couplings of Fe–Mn–Si–Ni–Cr shape memory alloys*, J. Mater. Design **56**:878. doi: 10.1016/j.matdes.2013.11.032.

5. Sawaguchi T., Maruyama T., Otsuka H., Kushibe A., Inoue Y., Tsuzaki K, (2016). *Design Concept and Applications of FeMnSi-Based Alloys from Shape-Memory to Seismic Response Control*, Mater. Trans., **57**(3), 283 – 293. doi.org/10.2320/matertrans.MB201510.

6. Pricop B., Söyler A.U., Özkal B., Bujoreanu L.G., (2020). *Powder Metallurgy: An Alternative for FeMnSiCrNi Shape Memory Alloys Processing*, Front. Mater. **7**:247, doi: 10.3389/fmats.2020.00247.

7. Pricop B., Mihalache E., Stoian G., Borza F., Özkal B., Bujoreanu L.G., (2018). *Thermo-mechanical effects caused by martensite formation in powder metallurgy FeMnSiCrNi shape memory alloys*, Powder Met., **61**(4), 348-356, doi: 10.1080/00325899.2018.1492773.

8. Pricop B., Borza F., Ozkal B., Bujoreanu L.G., (2021). *Influence of Thermal and Mechanical/Powder Processing on Microstructure and Dynamic Stiffness of Fe-Mn-Si-Cr-Ni Shape Memory Alloy*, Trans Indian Inst Met., 74(6), 1409-1418, doi: 10.1007/s12666-021-02215-8.

9. Ciurca L., Lohan N.M., Pricop B., Bujoreanu L.G., (2019). *Study of tensile behaviour of Fe base shape memory alloys during mechanical cycling*, IOP Conf. Ser.: Mater. Sci. Eng. 591 012009, doi:10.1088/1757-899X/591/1/012009.

10. Ciurcă L., Pricop B., Agop M., Bujoreanu L.G., (2022). *On bending creep behaviour of a powder metallurgy FeMnSiCrNi shape memory alloy*, *Archives of Metallurgy and Materials*, doi: 10.24425/amm.2022.139681.

11. Soyler A.U., Özkal B., Bujoreanu L.G., (2010).

Sintering Densification and Microstructural Characterization of Mechanical Alloyed Fe-Mn-Si based Powder Metal System, Supplemental Proceedings, Vol. **3**. General Paper Selections TMS, (The Minerals, Metals & Materials Society), 785-792.
12. Soyler A.U., Özkal B., Bujoreanu L.G., (2011). *Investigation of Mechanical Alloying Process Parameters on Fe-Mn-Si Based System*, Supplemental Proceedings, Vol. **1**. Materials Processing and Energy Materials TMS, (The Minerals, Metals & Materials Society), 577-583.
13. Soyler A.U., Özkal B., Bujoreanu L.G., (2014). *Improved Shape Memory Characteristics of Fe-14Mn-6Si-9Cr-5Ni Alloy Via Mechanical Alloying*, J Mater Eng Perform, **23**, 2357–2361.
14. Pricop B., Özkal B., Söyler U., Van Humbeeck J., Lohan N.M., Suru M.G., Bujoreanu L.G., (2014). *Influence of mechanically alloyed fraction and hot rolling temperature in the last pass on the structure of Fe-14Mn-6Si-9Cr-5Ni (mass. %) shape memory alloys processed by powder metallurgy*, Optoelectron Adv M, **8**(3-4), 247 – 250.
15. Leinenbach C., Lee W.J., Lis A., Arabi-Hashemi A., Cayron C., Weber B., (2016). *Creep and stress relaxation of a FeMnSi-based shape memory alloy at low temperatures*, Mat. Sci. Eng. A, **677**, 106–115. doi.org/10.1016/j.msea.2016.09.042.
16. Reed R C, *The Superalloys Fundamentals and Applications*, Cambridge University Press, 2006, pp. 33-120.
17. Pricop B., Mihalache E., Lohan M.N., Istrate B., Mocanu M., Ozkal B., Bujoreanu L.G., (2015). *Powder metallurgy and mechanical alloying effects on the formation of thermally induced martensite in an FeMnSiCrNi SMA*, MATEC Web of Conferences, **33**, 04004.
18. Kajiwara S., (1999). *Characteristic features of shape memory effect and related transformation behavior in Fe-based alloys*, Mater. Sci. Eng. A **273-275**, 67-88.

Received: April 13, 2022 / Accepted: June 15, 2022 / Paper available online: June 20, 2022 © International Journal of Modern Manufacturing Technologies